

An Optimized Binning and Probabilistic Slice Sharing Algorithm for Motion Correction in Abdominal DW-MRI

Michelle Su^{1,2*}, Serge Vasylechko¹, Cemre Ariyurek¹, Onur Afacan¹, Sila Kurugol¹

¹Boston Children's Hospital, Harvard Medical School

²Lincoln-Sudbury Regional High School

*michelle.su@childrens.harvard.edu

Abstract. Abdominal diffusion-weighted magnetic resonance imaging (DW-MRI) is a powerful, non-invasive technique for characterizing lesions and facilitating early diagnosis. However, respiratory motion during a scan can degrade image quality. Binning image slices into respiratory phases may reduce motion artifacts, but when the standard binning algorithm is applied to DW-MRI, reconstructed volumes are often incomplete because they lack slices along the superior-inferior axis. Missing slices create black stripes within images, and prolonged scan times are required to generate complete volumes. In this study, we propose a new binning algorithm to minimize missing slices. We acquired free-breathing and shallow-breathing abdominal DW-MRI scans on seven volunteers (age 36.7 ± 4.2 years) and used our algorithm to correct for motion in free-breathing scans. First, we drew the optimal rigid bin partitions in the respiratory signal using a dynamic programming approach, assigning each slice to one bin. We then designed a probabilistic approach for selecting some slices to belong in two bins. Our proposed binning algorithm resulted in significantly fewer missing slices than standard binning ($p < 1.0 \times 10^{-16}$), yielding an average reduction of $82.98 \pm 6.07\%$. Our algorithm also improved lesion conspicuity and reduced motion artifacts in DW-MR images and Apparent Diffusion Coefficient (ADC) maps. ADC maps created from free-breathing images corrected for motion with our algorithm showed lower intra-subject variability compared to uncorrected free-breathing and shallow-breathing maps ($p < 0.001$). Additionally, shallow-breathing ADC maps showed more consistency with corrected free-breathing maps rather than uncorrected free-breathing maps ($p < 0.01$). Our proposed binning algorithm's efficacy in reducing missing slices increases anatomical accuracy and allows for shorter acquisition times compared to standard binning.

1 | Introduction

Abdominal diffusion-weighted magnetic resonance imaging (DW-MRI) has been shown to enhance evaluations of disease progression and oncological treatment response^{1,2}. DW-MRI measures the Brownian motion of water molecules in tissues. Volumes with varying diffusion-weighting gradients (b-values) are acquired to enable the computation of apparent diffusion coefficient (ADC) values³. ADC values are valuable biomarkers for early detection and characterization of lesions such as hepatic focal lesions such as hepatocellular carcinoma (HCC) and metastases⁴⁻⁷. DW-MRI techniques are also effective

in assessing small satellite lesions in the liver, splenic lesions, and renal cell carcinoma in (RCC) in the kidneys^{4,8}.

However, respiratory motion can significantly diminish the quality of images and ADC maps⁹, especially in pediatric or anxious patients, who often exhibit deep or irregular respiration¹⁰. Clinical approaches to motion correction in abdominal MRI include breath-holding and respiratory gating. With the breath-holding method, scan time is restricted to how long a patient can hold their breath for¹¹. This approach thus limits the spatial coverage, the signal-to-noise ratio (SNR), and the number of volume averages and directions. Additionally, breath-holding is infeasible for non-cooperative patients such as young children. With respiratory gating, a belt or navigator records the respiratory signal, and images are acquired only when the respiratory signal falls within a certain gate^{12,13}. Since the signal typically falls within the gate 30% of the time, gating requires prolonged scan times and may still produce images with residual motion¹⁴.

Alternatively, techniques for motion measurement and correction based on 2D non-rigid registration can be applied to abdominal DW-MRI. However, these techniques only correct for in-plane motion and ignore through-plane motion in the superior-inferior direction, which is the direction most affected by respiratory motion^{15,16}. There are also 3D non-rigid registration-based techniques for motion correction¹⁷⁻¹⁹. However, performance is limited because the thick slices in abdominal DW-MRI cause a low superior-inferior resolution, and contrast differences exist between images acquired at different b-values. Another alternative is 3D slice-to-volume registration (SVR) techniques, but these techniques only correct for rigid motion rather than non-rigid motion^{20,21}.

Binning into respiratory phases has proven to be an effective motion correction method for T1-weighted MRI²²⁻²⁴. In recent works, binning has also been used to correct for respiratory motion in DW-MRI. Each image slice is sorted into one motion state (or bin) based on its corresponding value in the respiratory signal obtained from a navigator^{25,26}. The standard binning method assigns an equal number of slices to each bin²⁷ without considering the slice and b-value information of those slices. Images within each bin are averaged to improve SNR. At each b-value, volumes constructed from each bin are aligned via 3D non-rigid registration, and these volumes are then averaged to produce one motion-corrected volume, further improving SNR. Binning requires shorter scan times to achieve comparable SNR with gating, as it acquires data during the entire respiratory cycle rather than acquiring data in just 30% of the respiratory cycle. Additionally, when non-rigid registration is employed to align bins, both rigid and non-rigid motion are addressed.

In comparison to other MRI sequences, DW-MRI poses a unique challenge for binning. After binning, a complete volume containing all slices should be generated at each bin and for each b-value. However, due to the inability to control respiration during free-breathing acquisitions, a patient's breathing may synchronize with sequence parameters. Consequently, DW-MR volumes in some bins often lack slices at certain locations along the superior-inferior axis, leading to black stripes in images and failing to represent the complete volumes necessary for non-rigid registration. The number of missing slices increases when a larger number of motion bins is used to accommodate deep breathing. Reducing missing slices requires extending acquisition time, which is undesirable in clinical practice.

To address these issues, we design a new binning method that results in fewer missing slices compared to the standard binning method, improving scan efficiency. Our two main contributions are as follows:

- 1) An algorithm optimizing initial motion state bin assignments to minimize the total number of missing slices using dynamic programming.
- 2) A bin assignment refinement algorithm for probabilistic slice sharing, which further reduces the number of missing slices.

Additionally, we experiment with a Pilot Tone (PT) navigator that allows for more accurate tracking of physiological motion than traditional navigators²⁸⁻³². We design a method for selecting the best PT channel from the multi-channel PT data using SNR-based criteria. For equal comparisons, we utilize the PT navigator to record the respiratory signal that is used by both the standard and proposed binning methods.

Our binning method aims to reduce the need to interpolate missing slices, increase anatomical accuracy, and shorten acquisition times compared to standard binning while maintaining motion-correction capabilities. We aim to produce motion-robust abdominal images with high lesion conspicuity, particularly for scans with irregular or deep breathing.

2 | Methods

2.1 Abdominal DW-MRI Study

A liver diffusion-weighted MRI clinical protocol was acquired on 7 volunteers (4 male, 3 female, age=36.7±4.2 years) who provided written informed consent for a protocol approved by an Institutional Board Review (IRB). Each subject participated in two scans. For the free-breathing (FB) scan, we instructed the subject to breathe deeply and allowed for irregular breathing patterns. For the shallow-breathing (SB) scan, we instructed the subject to remain relatively still and take breaths as shallow as possible. Subjects 6 and 7 had benign lesions.

DW-MR volumes (b-values = 50, 400, 800 s/mm² with 3, 3 and 4-5 averages respectively and 6 directions) were collected in each scan using a 3T scanner (MAGNETOM PRISMA/VIDA, Siemens Healthineers, Erlangen, Germany). We used a free-breathing single-shot echo planar imaging (EPI) sequence. The imaging parameters were TE = 78 ms, TR = 5200 ms, FOV = 380x310mm², in-plane resolution of 1.5x1.5mm², number of slices (N_{sl}) = 42-52, slice thickness = 4mm, bandwidth = 2442 Hz/px, total scan time = 5.2 minutes. A Pilot Tone (PT) device³³ was placed on the patient table near the hip of each volunteer to record motion during FB scans. We saved the raw k-space data and extracted the corresponding PT navigator signal from each channel²⁹.

2.2 Pilot Tone Channel Selection

To select the PT channel most representative of physiological motion, we proposed a method to select the channel with the highest SNR. We first removed any linear trend in each extracted signal to prevent the PT drift from distorting our motion signal. We subtracted a linear least-squares regression line from the data and shifted the minimum signal to 0. We then selected the navigator signal with the highest SNR, defined as $SNR = \log_{10} \left(\frac{\mu_o}{\mu_{o-D}} \right)$. O denotes the original signal, and D represents the denoised signal. D is the result of applying a zero-padded median filter on O with a kernel size of 5.

2.3 Missing Slice Problem and Solution

A missing slice occurs when a reconstructed volume V with b-value b_v and motion state number m_v does not contain at least one slice for every slice number 0 to $S-1$. We have a total of NDW -MRI slices across all combined volumes of the scan. A single slice i possesses a corresponding value for its PT signal p_i , b-value $b_i \in \{50, 400, 800\}$, and slice number $s_i \in \{0, 2, 3, \dots, S-1\}$. Our proposed binning algorithm divides the N slices into K bins based on the PT signal, where each bin contains slices corresponding to one respiratory motion state. We subsequently generate $3 \times K$ total volumes, with one volume for each b-value and motion state bin. A missing slice is defined as a combination of (motion state m_s , b-value b_s , slice number s_s) where no data falls. Our algorithm is designed to minimize the total number of missing slices across the $3 \times K$ volumes. The initial optimal bin assignment step assigns each slice to one bin, creating the optimal rigid bin partitions. The probabilistic slice sharing step allows selective slices to be shared between bins.

2.4 Initial Optimal Bin Assignment

We first assigned each slice to one bin to design the initial rigid bin partitions for minimizing the total number of missing slices. This step of our algorithm returned the optimal bin assignments for each slice based on the global minimum for the number of missing slices across all $3 \times K$ volumes. We defined our objective function to be the total missing slices. Minimizing the missing slices was equivalent to maximizing the total number of combinations of (b-value, slice number) covered by the slices in each bin. Our process was described as follows.

We sorted all slices by increasing PT signal value. We precomputed an $N \times 3 \times S$ prefix sum array. Each $3 \times S$ subarray in this array stored the number of slices existing for each combination (b-value, slice number) between the slice at index 0 until the slice at given index $i \in \{0, 2, 3, \dots, N-1\}$ in the sorted list. We used the precomputed to find $R_{(i, n)}$, denoting the number of missing slices in the range of slices $[i, n)$ in the sorted slice list. Our dynamic programming algorithm utilized two $K \times N$ arrays to respectively store the minimum objective function value $F_{(k, n)}$ and the corresponding partition point for the last bin for a given k and n . We used a tabulation approach to fill these two arrays. For each combination of k and n , we iterated through each possible last partition point $i \in \{0, 2, 3, \dots, N-1\}$. We minimized the sum of the objective function to left of the partition, $F_{(k-1, i)}$, and the objective function to the right of the partition, $R_{(i, n)}$:

$$F_{(k, n)} = \operatorname{argmin}(i) (F_{(k-1, i)} + R_{(i, n)}) \quad (1)$$

We used a memoization approach to reconstruct the partition points for our final K and N . The time complexity of our algorithm is $O(K * N^2)$.

2.5 Probabilistic Slice Sharing

We then selected a small portion of slices to be shared between two bins, reducing the missing slices that remain after the initial optimal bin assignment. This process allowed the shared slices to form an exception to the initially rigid bin partitions. We first constructed a Gaussian model for each bin. For each combination of $slice_i$ and bin_j , we computed the probability density $PD_{(i, j)}$ that $slice_i$ belongs to bin_j using the Gaussian model for bin_j . We weighted each $PD_{(i, j)}$ by the number of slices in bin_j to

produce a weighted density $W_{(i,j)}$. For each $slice_i$, we computed a set of probabilities $P_{(i)} \in \{p_{(i,0)}, p_{(i,1)}, \dots, p_{(i,k-1)}\}$. Each $p_{(i,j)}$ was defined as $p_{(i,j)} = \frac{W_{(i,j)}}{\sum_{k=1}^K W_{(i,k)}}$, representing the normalized probability that $slice_i$ belongs to bin_j . These first few steps share parallels with the expectation step of the expectation-maximization (EM) algorithm for Gaussian Mixture Modeling³⁴. We used the bin assignments from the binning step as an initialization for the slice sharing step. For each bin_j , each missing $slice_i$ was characterized by a combination (motion state m , b-value b , slice number s). We identified the candidate slices to fill each missing slice. A candidate slice was defined as being currently assigned to bin bin_c but holding the potential to fill this missing slice if also assigned to bin_f .

We proposed a share metric to determine the plausibility for a slice to belong to two bins. For $slice_i$, the share metric was defined as $SM_i = \frac{p_{(i,D)}}{p_{(i,c)}}$, where bin_c is the initial bin assignment and bin_f is the bin with a missing slice to be filled. We selected the optimal slice to fill a missing slice as the candidate slice with the greatest share metric with the constraint that a candidate slice cannot fill more than one missing slice. We filled a missing slice $slice_i$ with its candidate slice (i.e. assign the candidate slice to both bin_c and bin_f) if the $SM_i > T$, where T is the share metric threshold. In addition to filling missing slices that meet this share metric threshold, we guaranteed that in a consecutive pair of missing slices, at least one of the slices in the pair was filled regardless of its share metric. This same process applied to missing slices at the edges of volumes. We selected the optimal K as the maximum K allowing for less than 2% of slices across all volumes to be missing after slice sharing.

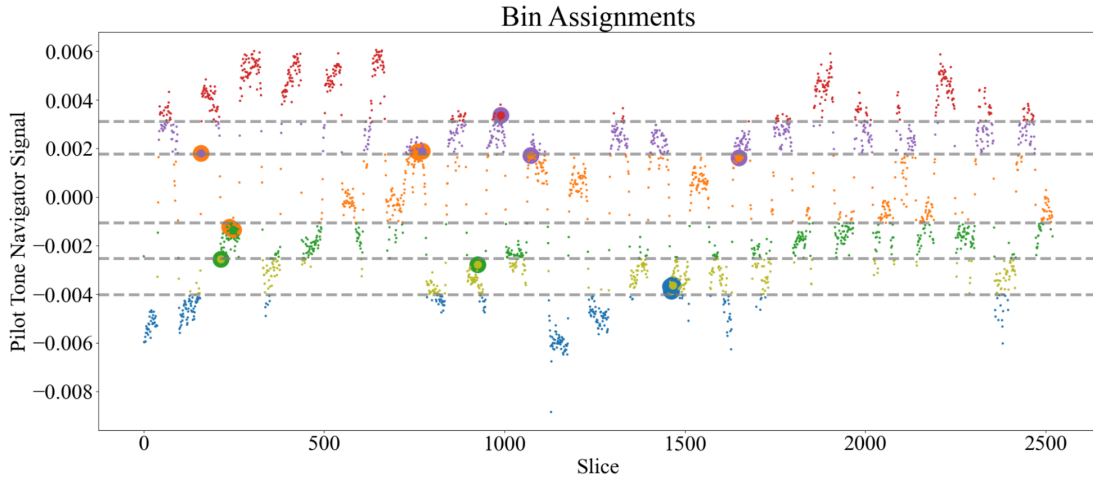


Figure 1. The final bin assignments using the proposed method are given for Subject 1 with $K = 6$ and $T = 0.1$. The gray lines denote the bin partitions from the initial optimal bin assignment step. The enlarged points represent the shared slices determined by probabilistic slice sharing, with the inner color denoting the initial bin assignment and the outer color denoting the second bin assignment.

2.6 Image Reconstruction and ADC Estimation

We applied this binning process to correct for motion in the free-breathing (FB scans). We sorted the data based on all combinations of motion state m_p , b-value b_p , slice number s_i . For combinations (m_p, b_p, s_i) that contained no data, we filled these remaining missing slices using linear interpolation. Each slice was only interpolated from its two nearest neighbors, as we had eliminated missing pairs of consecutive slices. (Non-rigid registration does not work with missing slices.) For combinations (m_p, b_p, s_i) that contained multiple slices, we averaged the multiple slices to enhance SNR. We therefore had one slice per combination (m_p, b_p, s_i) . Using the final bin assignments, we generated one volume for each b-value of each bin, resulting in $3 \times K$ total volumes. We performed isotropic resampling on each volume to match the higher resolution of the axial image to the coronal and sagittal resolutions.

For each b-value (b50, b400, and b800), we registered $K-1$ floating motion state volumes to one reference motion state volume using an automated diffeomorphic non-rigid transformation³⁵. We selected the reference volume to be the end-expiration motion state, as during end-expiration, the abdomen appears largest and motion is at a minimum^{36,37}. The end-expiration motion state was either bin_0 or bin_{K-1} depending on the orientation of the PT navigator signal. For subjects with lesions, we supplemented additional reconstructed volumes by selecting the fixed volume to be the motion state bin that displays the clearest view of a specified lesion. Following the non-rigid registration process, we resampled each isotropic volume to its original dimensions. We averaged the K registered motion state volumes for each b-value to produce a final motion-corrected free-breathing (MoCo FB) volume for each b-value.

We additionally generated uncorrected free-breathing (No MoCo FB) and uncorrected shallow-breathing (SB) volumes for comparison. We created uncorrected volumes by averaging the raw DW-MR volumes from repetitions of the 6 diffusion directions for each b-value. For MoCoFB, NoMoco FB, and NoMoCO SB, we used Singular Value Decomposition (SVD) to perform least squares fitting of a single exponential model decay model based on the 3 b-values at each voxel. We used the ADC parameter from the exponential decay model at each voxel to estimate ADC parameter maps.

3 | Results

3.1 Binning

We evaluated the number of missing slices resulting from the standard and proposed binning methods for free-breathing (FB) scans. The number of missing slices is the summation of the number missing slices across the $3 \times K$ volumes, with one volume per combination of b-value and motion-state bin. In the calculation of percentage of missing slices, the number of slices across all volumes is used as the total number of slices, which is equal to 3 (number of b-values) \times K (number of bins) \times nSli (number of slices). Compared to the standard binning method, the proposed binning method yielded an average of $82.98 \pm 6.07\%$ fewer missing slices across all subjects. With the initial optimal bin assignment step alone (without probabilistic slice sharing), the number of missing slices was reduced by an average of $36.76 \pm 0.10\%$ compared to the standard binning method. The proposed binning method resulted in an average of 8.57 ± 2.66 missing slices, or $0.87 \pm 0.27\%$ of all slices being missing slices. The standard binning method resulted in an average of 34.86 ± 11.64 missing slices, or $5.60 \pm 1.67\%$ of all slices being missing slices. A one-sided two-proportion z-test with the null hypothesis that the total proportion of missing

slices across all subjects is equal using standard binning and using the proposed binning method resulted in a p-value of less than 1.0×10^{-16} . Table 1 shows subject-specific results for the number of missing slices and the percentage of missing slices.

Subject		Sub. 1	Sub. 2	Sub. 3	Sub. 4	Sub. 5	Sub. 6	Sub. 7
Number of bins (K)		6	9	9	6	7	7	7
Number of missing slices (% of missing slices)	Standard binning	44 (5.82%)	68 (6.00%)	67 (5.91%)	27 (2.88%)	74 (7.34%)	41 (3.90%)	65 (7.34%)
	After proposed binning step 1	19 (2.51%)	48 (4.23%)	42 (3.70%)	19 (2.03%)	42 (4.20%)	28 (2.67%)	46 (5.22%)
	After proposed binning step 2	4 (0.53%)	10 (0.88%)	7 (0.62%)	7 (0.75%)	13 (1.29%)	9 (0.86%)	10 (1.14%)
Reduction in missing slices with proposed binning (%)		90.90	85.29	89.56	74.07	82.43	78.05	80.56

Table 1. The total number and percentage of missing slices resulting from binning using the optimal number of bins (K) is shown for the standard binning method and after each step of the proposed binning method for free-breathing (FB) scans. The percent reduction of the number of missing slices achieved by the proposed binning method is also shown. The proposed method consistently reduces the number of missing slices compared to the standard method, diminishing the need to extend scan time to fill missing slices.

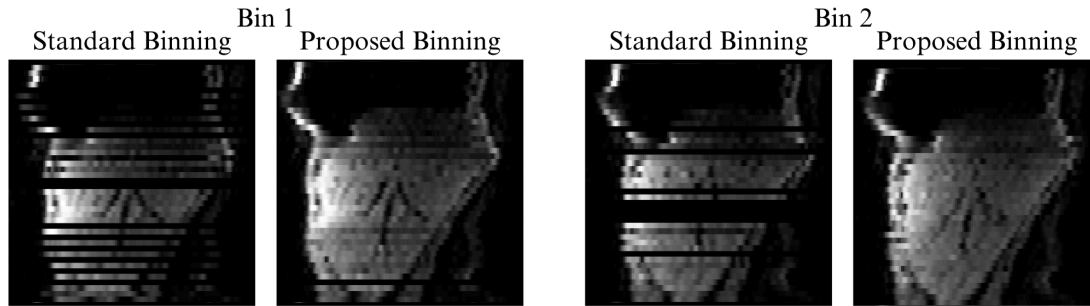


Figure 2. Subject 1 free-breathing (FB) b50 volumes for motion-state bins 1 and 2 are shown in the sagittal plane using results from the standard and proposed binning methods. These images were obtained prior to interpolation, registration, and averaging. The proposed method preserves the anatomical accuracy of each bin by eliminating large gaps with consecutive missing slices as well as isolated missing slices. This leads to more anatomically accurate final volumes, which result from bin volumes being registered and averaged together.

3.3 Qualitative Evaluation of Lesion Conspicuity and Image Quality

We observed image quality for the axial, coronal, and sagittal plane images of FB scans (Figure 3). Compared to NoMoCo images, MoCo axial images consistently reduced motion artifacts surrounding

the kidneys, liver, and spleen, particularly for the subjects exhibiting deep or irregular breathing patterns throughout the scan (Subjects 2 and 4). MoCo axial images of the liver also showed improved conspicuity of blood vessels. MoCo coronal and sagittal images showed reduced blurring and increased conspicuity of abdominal organ boundaries. (The black sections near the bottom of MoCo coronal and sagittal images are a result of non-rigid registration rather than missing slices.) We additionally observed lesion conspicuity in the 2 subjects with benign lesion(s) (Figure 4). For both MoCo and No MoCo images, the slice that provided the clearest view of the lesions was selected. For subject 6, motion artifacts obscure two of the three lesions are not visible in the No MoCo image. The MoCo image shows increased conspicuity for the single lesion in Subject 7.

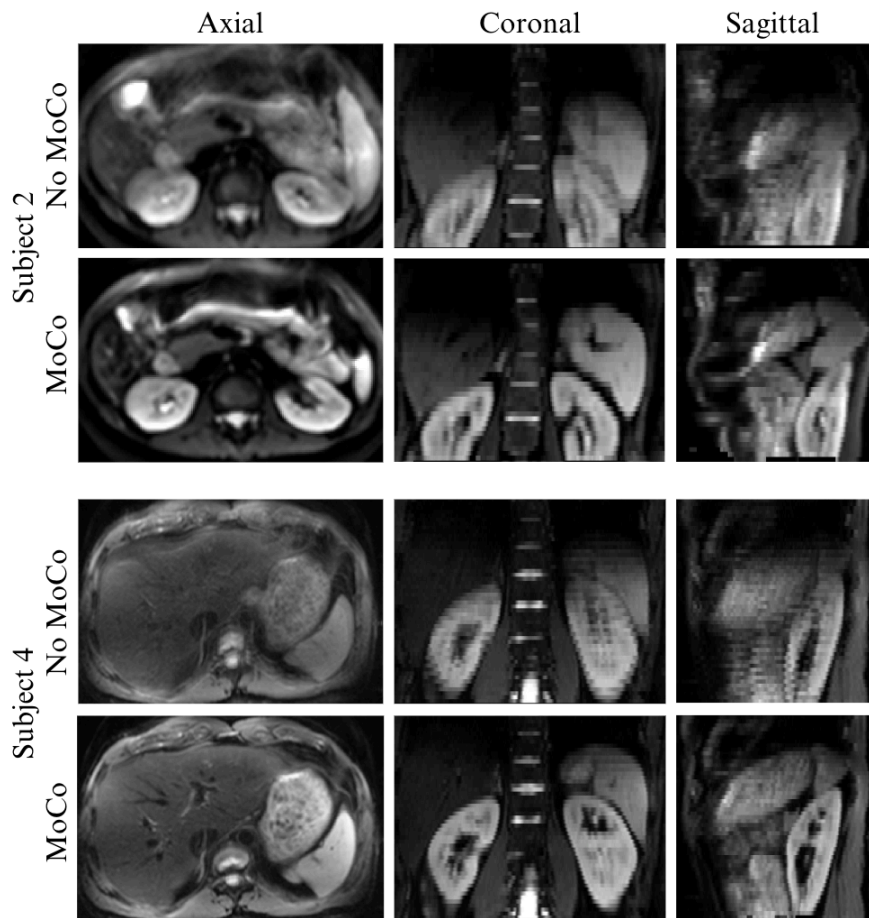


Figure 3. Subject 2 and Subject 4 free-breathing (FB) final b50 volumes are shown in the axial, coronal, and sagittal planes with the proposed motion correction method (MoCo) and without motion correction (No MoCo). These final images were obtained after registering and averaging all bins. MoCo images show increased conspicuity, reduced motion artifacts, and reduced blurring, which may allow clinicians to make more precise diagnoses.

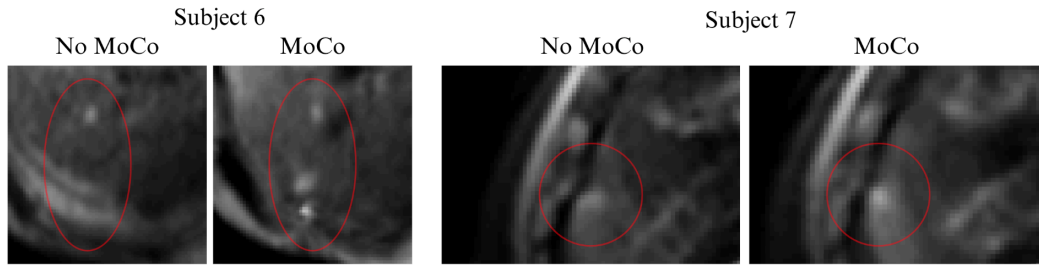


Figure 4. Benign lesions in Subject 6 and 7 free-breathing (FB) final b50 volumes are shown in the axial plane with the proposed motion correction method (MoCo) and without motion correction (No MoCo). These final images were obtained after registering and averaging all bins. MoCo images show improved lesion conspicuity, allowing for more accurate lesion characterization and treatment administration by clinicians.

3.2 Quantitative Evaluation of ADC Estimation

We evaluated our proposed binning method’s potential for estimating ADC maps by comparing motion-corrected free-breathing (MoCo FB) and uncorrected shallow-breathing (SB) ADC values. Additionally, we compare uncorrected free-breathing (No MoCo FB) and SB ADC values. We segmented three regions-of-interests (ROIs) in homogeneous and normal areas of the spleen, liver, and left kidney for each subject, resulting in 21 ROIs total across the 7 subjects. For these ROI segmentations, we created one 2D 64-voxel mask for the MoCo and No MoCo FB scans and created a corresponding 64-voxel mask for the SB scans by matching biomarkers around each ROI between FB and SB scans. The violin plots in Figure 5 compare mean and standard deviation for ADC values in the ROIs of each subject.

We computed two metrics based on ROI ADC values to measure variability within subject ROIs and variability across subject ROIs. To measure intra-subject variability, we calculated the coefficient of variation (CoV) of ADC within a subject’s ROI. We then compared the mean of these CoVs between MoCo FB, No MoCo FB, and SB images. The mean CoV of the 21 ROIs in MoCo FB images is 72.78% lower compared to No MoCo FB images and 58.51% lower compared to SB images. The mean CoVs of each ROI type (spleen, liver, and kidney) are also lowest in MoCo FB images. One-sided two-sample t-tests (unequal variances) for a negative difference in mean CoV between (i) MoCo FB and SB and (ii) MoCo FB and NoMoCo FB both yielded p-values of less than 0.001. This indicates that MoCo FB ADC values show less intra-subject variability, indicating higher precision in ADC values. Additionally, we used a separate metric to measure inter-subject variability. We first computed the mean ADC value in a subject’s ROI, and we then found the CoV of the mean ADC values across different subjects. We compared the CoV of mean ADC across subjects between MoCo FB, No MoCo FB, and SB images. For ROIs of each type and for all 21 ROIs combined, the CoV of mean ADC values across the 7 subjects is lower for MoCo FB than SB and NoMoCo FB, indicating less variability in ADC values across subjects. For the 21 ROIs, the CoV of mean ADC values across the 7 subjects in MoCo FB images is 63.91% lower compared to No MoCo FB images and 45.07% lower compared to SB images. Table 2 provides additional data on these metrics.

Additionally, we computed two metrics to characterize the resemblance between (i) MoCo FB and SB images and (ii) NoMoCo FB and SB images. For each ROI, we also computed the Wasserstein distance and the root-mean-square error (RMSE) between the MoCo FB and SB images as well as No MoCo FB and SB images. For each ROI type individually and for all ROIs, the mean Wasserstein distances and RMSE values were consistently lower between MoCo FB and SB compared to No MoCo FB and SB. On average, Wasserstein distances were 50.00% lower between MoCo FB and SB, and RMSE values were 42.68% lower between MoCo FB and SB. Four one-sided two-sample t-tests (unequal variances) for a negative difference in these metrics between (i) MoCo FB and SB images and (ii) NoMoCo FB and SB images each yielded p-values of less than 0.01. This demonstrates that SB images tend to be more similar to MoCo FB images than No MoCo FB images. Table 3 provides mean Wasserstein distance and RMSE values separated by ROI type.

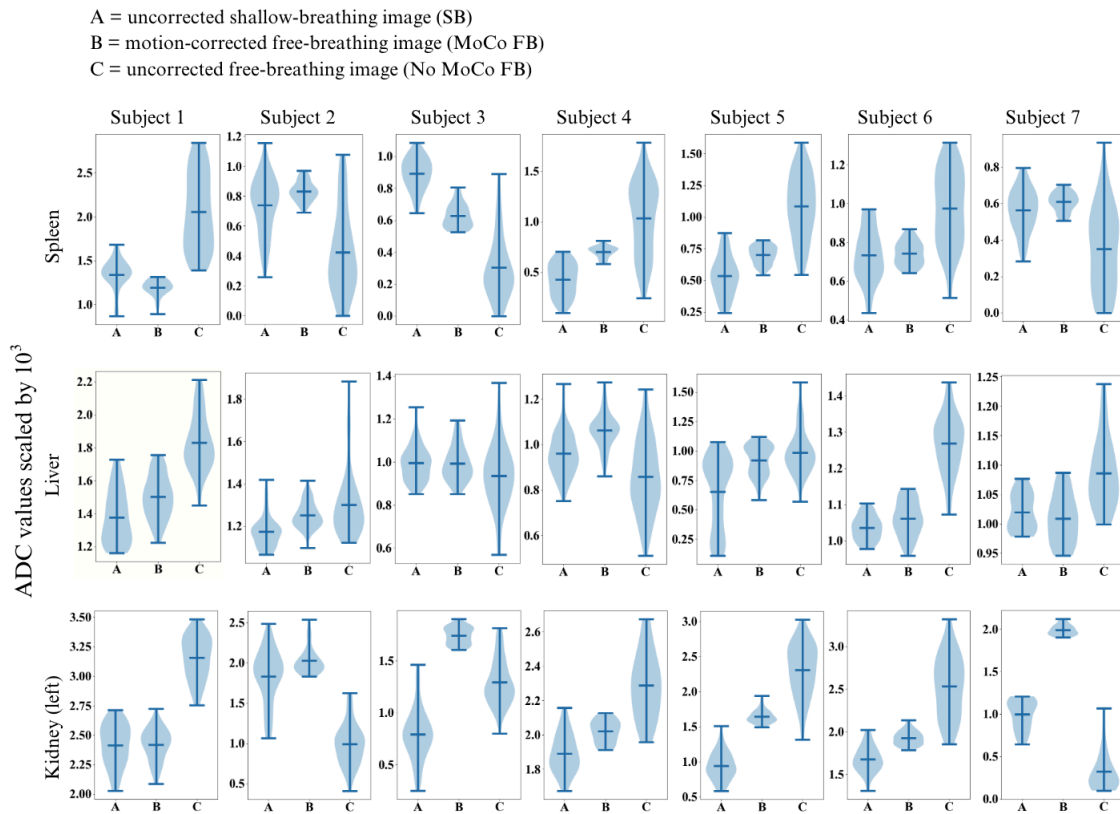


Figure 5. Violin plots of ADC values scaled by 10^3 are shown for each of the three 2D 64-voxel homogeneous ROI segmentations (spleen, liver, and left kidney) for the 7 healthy subjects. Mean \pm SD values are shown. ADC values are compared for uncorrected shallow-breathing (SB), motion-corrected free-breathing (MoCo FB), and uncorrected free-breathing images (No MoCo FB). Mean ADC values tend to be closer between SB and MoCo FB than between SB and No MoCo FB. These results may elucidate the ability of the proposed motion-correction method to reduce artifacts in FB scans and render them more similar to SB scans. Standard deviation of ADC values are lowest in MoCo FB images,

indicating less variability within the homogeneous ROIs, which may be caused by a reduction in motion artifacts.

	Intra-subject Variability: Mean CoV of ADC in ROIs (%)			Inter-subject Variability: CoV of mean ADC across subjects (%)		
	SB	MoCo FB	No MoCo FB	SB	MoCo FB	No MoCo FB
Spleen ROIs	22.43	8.80	42.65	40.68	25.68	69.17
Liver ROIs	12.77	7.43	12.25	21.28	17.86	27.99
Kidney ROIs	15.88	4.96	22.95	40.20	12.58	54.14
All ROIs	17.03	7.06	25.95	34.05	18.71	50.43

Table 2. The mean coefficient of variation (CoV) of ADC within subject ROIs, measuring intra-subject variability, is shown for all ROI types. The CoV of mean ADC in ROIs across different subjects, measuring inter-subject variability, is also shown for all ROI types. The ROIs were selected from homogeneous areas of normal tissue, so low intra-subject and inter-subject variability is expected for motion-robust images. The mean CoV is lowest in motion-corrected free-breathing (MoCo FB) images, supporting the ability of the proposed binning method to reduce motion within ROIs. The CoV of mean ADC is lowest in MoCO FB images, indicating how the reduction in motion artifacts may be associated with more consistent ADC values across the subjects.

	Mean ADC Wasserstein distance		Mean ADC root mean square error (RMSE)	
	MoCo FB to SB	No MoCo FB to SB	MoCo FB to SB	No MoCo FB to SB
Spleen ROIs	1.59×10^{-4}	4.63×10^{-4}	2.41×10^{-4}	5.71×10^{-4}
Liver ROIs	8.92×10^{-5}	1.98×10^{-4}	1.74×10^{-4}	2.78×10^{-4}
Kidney ROIs	4.66×10^{-4}	7.68×10^{-4}	5.48×10^{-4}	8.32×10^{-4}
All ROIs	2.38×10^{-4}	4.76×10^{-4}	3.21×10^{-4}	5.60×10^{-4}

Table 3. The mean Wasserstein distances and root mean square error (RMSE) values are compared between (i) shallow breathing (SB) and motion-corrected free-breathing (FB) and (ii) SB and uncorrected free-breathing (No MoCo FB). The former type of comparison yields lower Wasserstein distances and RMSE values for each ROI type individually and for all ROIs. This reveals the ability of the proposed binning method to correct for motion in free-breathing images and make them more similar to shallow-breathing images.

4 | Discussion

The proposed binning method results in an average of only 0.87% total slices missing, compared to an average of 5.60% total slices missing with the standard uniform binning method. The proposed method additionally eliminates any consecutive missing slices. In contrast, the standard method's 5.60% missing slices reduces anatomical accuracy because missing slices must be interpolated before 3D non-rigid registration. Given that each slice is approximately 4mm thick, multiple consecutive missing slices can create substantial gaps. Interpolation methods cannot recover lesions that fall within gaps, potentially resulting in partial or whole lesions being lost. When bins are registered and averaged together, even one bin that fails to represent a lesion can blur the lesion in the averaged image. Missing slices are frequently unevenly distributed across bins, so one or more particularly low-quality bins can easily ruin averaged images. The proposed binning method addresses this issue by reducing missing slices in all bins, and ensuring a relatively uniform distribution of the few remaining missing slices across bins. Thus, the first advantage of the proposed binning method is maintaining the anatomical accuracy in the kidney, liver, and spleens, especially concerning lesions.

The proposed binning method also requires shorter scan times than the standard method. In order to preserve anatomical accuracy with the standard binning method, scan times would need to be extended, as the combinations of motion state, b-value, slice number that exist depend entirely on the subject's respiration. To fill missing slices, an unnecessary amount of repeated data in slices that already have one or multiple images would be acquired. The proposed binning method maximizes data utilization, making it a much more viable option for clinical translation.

Visual comparisons between images corrected for motion using the proposed binning method (MoCo) and uncorrected images (No MoCo) demonstrate the motion-correction capability of the proposed method. Standard uniform binning has previously been shown to successfully correct for motion in types of MRI other than DW-MRI. Due to the issue of anatomical inaccuracies with standard binning, we focus on evaluating the proposed binning method for MoCo. No MoCo images for free-breathing (FB) scans show significant motion artifacts and blurring. However, MoCo images in the three available planes (axial, coronal, and sagittal) show little visible motion, clear organ boundaries, and more anatomical details. MoCo axial images can also reveal benign lesions that do not appear in No MoCo images and improve the conspicuity of benign lesions that appear blurred in No MoCo images. Therefore, these axial images may prove especially useful for clinicians to analyze lesions and improve diagnosis capability. No MoCo sagittal and coronal images show extensive motion in the superior-inferior direction in free-breathing (FB) scans, but such motion is eliminated or significantly reduced in MoCo images. The high image quality of sagittal and coronal images demonstrates that the slices are correctly ordered and confirms the legitimacy of motion correction in the axial plane. In future work, we intend to evaluate our method in subjects with malignant lesions.

Quantitative analysis of ADC estimations in homogeneous ROIs support the efficacy of the proposed binning method. Analysis using coefficients of variation of ADC values indicate that compared to both uncorrected shallow-breathing (SB) and uncorrected FB (No MoCo FB) images, motion-corrected FB images (MoCo FB) show lower intra-subject and inter-subject variability. Since we selected the ROIs to be homogeneous, we expect low intra-subject variability in motion-robust images. We also expect low inter-subject variability in motion-robust images because the ROIs are normal and

healthy in across the 7 volunteers. These results elucidate the increased stability of the ADC parameter when our motion correction method is used. It is essential for ADC to be stable in homogeneous regions so that clinicians can track areas with lower ADC to correctly detect lesions. The lower variability of MoCo FB compared to SB indicates that SB scans may still be affected by some degree of motion and that motion correction eliminates effects of both deep and shallow breathing. In other words, MoCo FB may be closer to the ground truth than SB. Although SB cannot be used as a perfect ground truth, analysis using Wasserstein distances and RMSE calculations indicate that MoCo FB and SB show more similar ADC values than No MoCo FB and SB.

A limitation of the proposed binning method is its slower speed in comparison to the standard method. For $K = 10$ (10 bins), the proposed method takes approximately 20 minutes, with variations depending on the length of the acquisition and the number of slices in the field of view, while the standard method takes less than one minute. However, due to the dynamic programming structure of the proposed method, when the proposed method runs for x bins, it produces all binning results from $K = 2$ to $K = x$. This system of cumulative results decreases the time spent for running different values of K . Additionally, this allows an automated algorithm to select the optimal number of bins K for a value less than or equal to x . With the standard method, binning must be executed for each individual K , and results are not cumulative. The speed of the proposed binning method has the potential to be reduced with future work involving parallel computations. Future work can also involve optimizing the number of bins based on a subject's depth of breathing. We used higher values of K in this work, but fewer bins may be used for clinical acquisitions with shorter scan times.

5 | Conclusion

In this study, we propose a new respiratory motion state binning method to minimize the number missing slices in reconstructed DW-MRI volumes while correcting for motion. Our proposed binning algorithm optimizes initial bin partitions and utilizes a probabilistic design to designate slices to be shared between neighboring bins. Our algorithm results in fewer missing slices compared to the standard uniform binning method. This reduces the need for slice interpolation, increases anatomical accuracy, and allows for shorter acquisition times. Our algorithm also successfully eliminates motion artifacts and improves lesion conspicuity, illustrating the potential for respiratory binning to be used in DW-MRI.

Acknowledgements

This work was supported partially by the National Institute of Diabetic and Digestive and Kidney Diseases (NIDDK), National Institute of Biomedical Imaging and Bioengineering (NIBIB), National Institute of Neurological Disorders and Stroke (NINDS) and National Library of Medicine (NLM) of the National Institutes of Health under award numbers R01DK125561, R21DK123569, R21EB029627, R01NS121657, R01LM013608, R01NS133228, and by the grant number 2019056 from the United States-Israel Binational Science Foundation (BSF), and a pilot grant from National Multiple Sclerosis Society under Award Number PP-1905-34002. We thank the Center for Advanced Imaging Innovation and Research (CAI2R) at NYU for supplying the 3T Pilot Tone device used in this work.

References

1. Serai SD. Basics of magnetic resonance imaging and quantitative parameters T1, T2, T2*, T1rho and diffusion-weighted imaging. *Pediatr Radiol.* 2022;52(2):217-227. doi:10.1007/s00247-021-05042-7
2. Caro-Domínguez P, Gupta AA, Chavhan GB. Can diffusion-weighted imaging distinguish between benign and malignant pediatric liver tumors? *Pediatr Radiol.* 2018;48(1):85-93. doi:10.1007/s00247-017-3984-9
3. Charles-Edwards EM, deSouza NM. Diffusion-weighted magnetic resonance imaging and its application to cancer. *Cancer Imaging.* 2006;6(1):135-143. doi:10.1102/1470-7330.2006.0021
4. Bonekamp S, Corona-Villalobos CP, Kamel IR. Oncologic applications of diffusion-weighted MRI in the body. *J Magn Reson Imaging.* 2012;35(2):257-279. doi:10.1002/jmri.22786
5. Abugamra S, Yassin A, Abdel-Rehim ASM, Sheha DS. Apparent diffusion coefficient for differentiating between benign and malignant hepatic focal lesions. *Egyptian Liver Journal.* 2020;10(1):1-8. doi:10.1186/s43066-020-00068-2
6. Afaq A, Andreou A, Koh DM. Diffusion-weighted magnetic resonance imaging for tumour response assessment: why, when and how? *Cancer Imaging.* 2010;10 Spec no A(1A):S179-S188. doi:10.1102/1470-7330.2010.9032
7. Galea N, Cantisani V, Taouli B. Liver lesion detection and characterization: role of diffusion-weighted imaging. *J Magn Reson Imaging.* 2013;37(6):1260-1276. doi:10.1002/jmri.23947
8. Sharma K, Agarwala S, Kandasamy D, et al. Role of Diffusion Weighted MRI (DW-MR) in Detection of Satellite Lesions Not Detected with Multiphase CT Scans in Hepatoblastoma and Its Implications for Management. *Indian J Pediatr.* 2022;89(10):968-974. doi:10.1007/s12098-021-04016-9
9. Axel L, Summers RM, Kressel HY, Charles C. Respiratory effects in two-dimensional Fourier transform MR imaging. *Radiology.* 1986;160(3):795-801. doi:10.1148/radiology.160.3.3737920
10. Chavhan GB, Babyn PS, Vasanawala SS. Abdominal MR imaging in children: motion compensation, sequence optimization, and protocol organization. *Radiographics.* 2013;33(3):703-719. doi:10.1148/rg.333125027
11. Paling MR, Brookeman JR. Respiration artifacts in MR imaging: reduction by breath holding. *J Comput Assist Tomogr.* 1986;10(6):1080-1082. doi:10.1097/00004728-198611000-00046
12. Li Q, Wu X, Qiu L, Zhang P, Zhang M, Yan F. Diffusion-weighted MRI in the assessment of split renal function: comparison of navigator-triggered prospective acquisition correction and breath-hold acquisition. *AJR Am J Roentgenol.* 2013;200(1):113-119. doi:10.2214/AJR.11.8052
13. Lewis CE, Prato FS, Drost DJ, Nicholson RL. Comparison of respiratory triggering and gating techniques for the removal of respiratory artifacts in MR imaging. *Radiology.* 1986;160(3):803-810. doi:10.1148/radiology.160.3.3737921

14. Kataoka M, Kido A, Yamamoto A, et al. Diffusion tensor imaging of kidneys with respiratory triggering: optimization of parameters to demonstrate anisotropic structures on fraction anisotropy maps. *J Magn Reson Imaging*. 2009;29(3):736-744. doi:10.1002/jmri.21669
15. Glutig K, Krüger PC, Oberreuther T, et al. Preliminary results of abdominal simultaneous multi-slice accelerated diffusion-weighted imaging with motion-correction in patients with cystic fibrosis and impaired compliance. *Abdom Radiol (NY)*. 2022;47(8):2783-2794. doi:10.1007/s00261-022-03549-7
16. Son JS, Park HS, Park S, et al. Motion-Corrected versus Conventional Diffusion-Weighted Magnetic Resonance Imaging of the Liver Using Non-Rigid Registration. *Diagnostics (Basel)*. 2023;13(6). doi:10.3390/diagnostics13061008
17. Kurugol S, Freiman M, Afacan O, et al. Motion-robust parameter estimation in abdominal diffusion-weighted MRI by simultaneous image registration and model estimation. *Med Image Anal*. 2017;39:124-132. doi:10.1016/j.media.2017.04.006
18. Kurugol S, Freiman M, Afacan O, et al. Motion Compensated Abdominal Diffusion Weighted MRI by Simultaneous Image Registration and Model Estimation (SIR-ME). *Med Image Comput Comput Assist Interv*. 2015;9351:501-509. doi:10.1007/978-3-319-24574-4_60
19. Mazaheri Y, Do RKG, Shukla-Dave A, Deasy JO, Lu Y, Akin O. Motion correction of multi-b-value diffusion-weighted imaging in the liver. *Acad Radiol*. 2012;19(12):1573-1580. doi:10.1016/j.acra.2012.07.005
20. Coll-Font J, Afacan O, Hoge S, et al. Retrospective Distortion and Motion Correction for Free-Breathing DW-MRI of the Kidneys Using Dual-Echo EPI and Slice-to-Volume Registration. *J Magn Reson Imaging*. 2021;53(5):1432-1443. doi:10.1002/jmri.27473
21. Kurugol S, Marami B, Afacan O, Warfield SK, Gholipour A. Motion-Robust Spatially Constrained Parameter Estimation in Renal Diffusion-Weighted MRI by 3D Motion Tracking and Correction of Sequential Slices. *Mol Imaging Reconstr Anal Mov Body Organs Stroke Imaging Treat (2017)*. 2017;10555:75-85. doi:10.1007/978-3-319-67564-0_8
22. Shahzadi I, Siddiqui MF, Aslam I, Omer H. Respiratory motion compensation using data binning in dynamic contrast enhanced golden-angle radial MRI. *Magn Reson Imaging*. 2020;70:115-125. doi:10.1016/j.mri.2020.03.011
23. Su M, Ariyurek C, Chow J, Afacan O, Kurugol S. Enhancing Motion Correction in T1-Weighted Abdominal MRI Through Outlier Removal and Overlapping Binning. In: *Proc. Intl. Soc. Mag. Reson. Med. 32 (2024)*. ; 2024.
24. Feng L, Axel L, Chandarana H, Block KT, Sodickson DK, Otazo R. XD-GRASP: Golden-angle radial MRI with reconstruction of extra motion-state dimensions using compressed sensing. *Magn Reson Med*. 2016;75(2):775-788. doi:10.1002/mrm.25665
25. Bush M, Vahle T, Krishnamurthy U, et al. Motion Correction of Abdominal Diffusion-Weighted MRI Using Internal Motion Vectors. In: *Proc. Intl. Soc. Mag. Reson. Med. 29 (2021)*. ; 2021.
26. Vasylychko S, Ariyurek C, Afacan O, Kurugol S. Respiratory binning with Pilot Tone Navigator For

Motion Compensated Liver DW-MRI. In: *Proc. Intl. Soc. Mag. Reson. Med.* 31 (2023). ; 2023.

27. Jhooti P, Gatehouse PD, Keegan J, Bunce NH, Taylor AM, Firmin DN. Phase ordering with automatic window selection (PAWS): a novel motion-resistant technique for 3D coronary imaging. *Magn Reson Med.* 2000;43(3):470-480. doi:10.1002/(sici)1522-2594(200003)43:3<470::aid-mrm20>3.0.co;2-u
28. Ariyurek C, Tess W, Kober T, Kurugol S, Afacan O. Comparison of k-space center, FID and Pilot Tone navigators in abdominal motion tracking for optimal XD-GRASP reconstruction. In: *Proc. Intl. Soc. Mag. Reson. Med.* 31 (2023). ; 2023.
29. Ariyurek C, Vasylechko S, Zhong X, et al. Pilot Tone-navigated motion estimation for liver DW-MRI. In: *Proc. Intl. Soc. Mag. Reson. Med.* 31 (2023). ; 2023.
30. Ludwig J, Speier P, Seifert F, Schaeffter T, Kolbitsch C. Pilot tone-based motion correction for prospective respiratory compensated cardiac cine MRI. *Magn Reson Med.* 2021;85(5):2403-2416. doi:10.1002/mrm.28580
31. Solomon E, Rigie DS, Vahle T, et al. Free-breathing radial imaging using a pilot-tone radiofrequency transmitter for detection of respiratory motion. *Magn Reson Med.* 2021;85(5):2672-2685. doi:10.1002/mrm.28616
32. Falcão MBL, Di Sopra L, Ma L, et al. Pilot tone navigation for respiratory and cardiac motion-resolved free-running 5D flow MRI. *Magn Reson Med.* 2022;87(2):718-732. doi:10.1002/mrm.29023
33. Schroeder L, Wetzl J, Maier A, et al. A Novel Method for Contact-Free Cardiac Synchronization Using the Pilot Tone Navigator. In: *Proc. Intl. Soc. Mag. Reson. Med.* 31 (2016). Accessed August 22, 2024. <https://archive.ismrm.org/2016/0410.html>
34. Reynolds D. Gaussian Mixture Models. *Encyclopedia of biometrics*. Published online October 18, 2018:659-663. doi:10.1007/978-0-387-73003-5_196
35. Commowick O, Wiest-Daesslé N, Prima S. Automated diffeomorphic registration of anatomical structures with rigid parts: application to dynamic cervical MRI. *Med Image Comput Comput Assist Interv.* 2012;15(Pt 2):163-170. doi:10.1007/978-3-642-33418-4_21
36. Vu KN, Haldipur AG, Roh ATH, Lindholm P, Loening AM. Comparison of End-Expiration Versus End-Inspiration Breath-Holds With Respect to Respiratory Motion Artifacts on T1-Weighted Abdominal MRI. *AJR Am J Roentgenol.* 2019;212(5):1024-1029. doi:10.2214/AJR.18.20239
37. Plathow C, Ley S, Zaporozhan J, et al. Assessment of reproducibility and stability of different breath-hold maneuvers by dynamic MRI: comparison between healthy adults and patients with pulmonary hypertension. *Eur Radiol.* 2006;16(1):173-179. doi:10.1007/s00330-005-2795-9